

Design, Fabrication and Analysis of a Mach-Zehnder Interferometer

Alfia Naaz Shaikh
Pramatra Tech Services (India) Private Limited
Bangalore, India
Email: alfia@pramatra.in

Abstract—This report details the design proposal for a set of Mach-Zehnder Interferometer (MZI) circuits intended for fabrication on a 220 nm silicon-on-insulator(SOI) platform using electron-beam lithography. The primary objective is to create structures that facilitate the accurate experimental extraction of the response of MZI compact models. One key parameter, the interferometer path length difference, is varied to target specific Free Spectral Ranges (FSRs). This proposal outlines the theoretical background of the Mach-Zehnder interferometer and its simulation results.

I. INTRODUCTION

A Mach-Zehnder Interferometer operates by splitting an input light beam into two separate paths, potentially introducing a relative phase shift between the paths, and then recombining the beams to produce interference. In its integrated form, an MZI typically comprises an input optical splitter (e.g., a Y-branch or directional coupler), two waveguide arms with lengths L_1 and L_2 , and an output optical combiner. The key parameter for the unbalanced MZI considered here is the physical path length difference $\Delta L = L_2 - L_1$. This path length difference introduces a wavelength-dependent phase difference $\Delta\Phi$ between the light propagating through the two arms.

II. THEORY- MZI TRANSFER FUNCTION

Consider an ideal MZI with lossless waveguides and perfect 50:50 power splitters and combiners. Let the input electric field be E_{in} . After the input splitter, the field entering each arm is $E_{in}/\sqrt{2}$.

The light propagates through the arms, accumulating phase shifts $\phi_1 = \beta L_1$ and $\phi_2 = \beta L_2$, where β is the propagation constant of the guided mode, given by

$$\beta(\lambda) = \frac{2\pi n_{eff}(\lambda)}{\lambda}$$

Ignoring propagation loss, the fields arriving at the input ports of the combiner are,

$$E_1 = \frac{E_{in}}{\sqrt{2}} e^{-i\beta L_1}$$

and

$$E_2 = \frac{E_{in}}{\sqrt{2}} e^{-i\beta L_2}$$

At the output combiner (assuming a symmetric 50:50 device like a Y-branch), the fields from the two arms interfere. The

combined field at the single output port, E_{out} , is proportional to the sum of the fields arriving from the two arms,

$$E_{out} = \frac{E_1 + E_2}{\sqrt{2}}$$

$$E_{out} = \frac{E_{in}}{2} (e^{-i\beta L_1} + e^{-i\beta L_2})$$

And the intensity is,

$$I_{out} = I_{in} \cos^2 \left(\frac{\beta \Delta L}{2} \right)$$

III. MODELLING AND SIMULATION

A. Waveguide Characterization

The simulations are based on the standard Silicon-on-Insulator (SOI) platform, featuring a crystalline silicon (Si) core layer with a fixed height $h = 220$ nm, a top and a buried oxide (BOX) layer on a silicon substrate. The upper cladding is made of silicon dioxide. The default waveguide width is $w = 500$ nm.

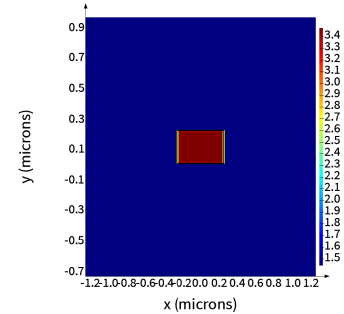


Fig. 1: Index profile of geometry

To study the mode profiles of the geometry, simulations are also performed using FDE MODE Solver from Ansys Lumerical. Simulations are conducted for the fundamental quasi-Transverse Electric (TE0) mode and the fundamental quasi-Transverse Magnetic (TM0) mode.

Consider the Taylor expansion around central wavelength, λ_0 for the effective index, n_{eff} as a function of wavelength,

$$n_{eff}(\lambda) = n_1 + n_2(\lambda - \lambda_0) + n_3(\lambda - \lambda_0)^2$$

where n_1, n_2, n_3, λ_0 are the parameters for the waveguide model. Running a frequency sweep over wavelength, a plot of

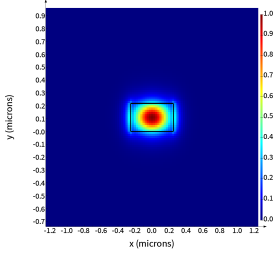


Fig. 2: TE polarization

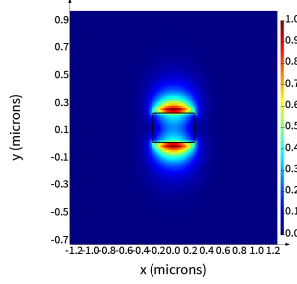


Fig. 3: TM polarization

Fig. 4: Comparison of TE and TM polarization.

effective index and group index of the waveguide is obtained with respect to wavelength.

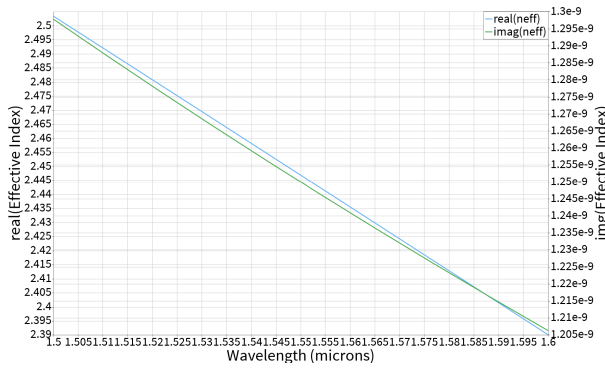


Fig. 5: Effective index variation

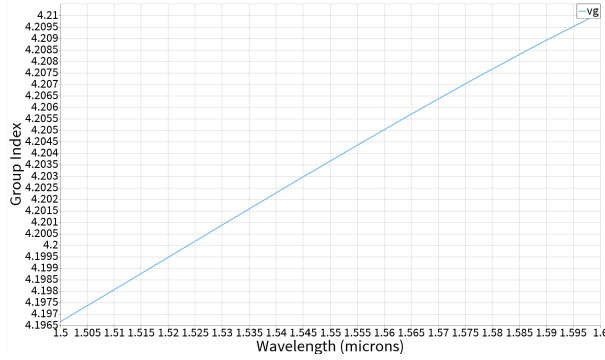


Fig. 6: Group index variation

B. Free Spectral Range (FSR)

The Free Spectral Range (FSR) is defined as the spacing in wavelength (or frequency) between adjacent transmission maxima (or minima) in the MZI spectrum. Therefore, the FSR for a MZI is given as,

$$FSR = \frac{\lambda^2}{n_g \Delta L}$$

This is the fundamental equation relating the measurable FSR to the group index n_g and the designed path length difference

ΔL at a given center wavelength λ . This derivation explicitly incorporates the group index, thereby accounting for the effect of waveguide dispersion on the FSR.

Experimentally, the FSR is measured from the transmission spectrum of the fabricated MZI at a specific center wavelength λ . The path length difference ΔL is a design parameter known from the device layout. Using these two values, the group index n_g at wavelength λ can be calculated. The simulation results of compact model for Mach-Zehnder with $\Delta L = 100 \mu\text{m}$ are shown below:

TABLE I: Free Spectral Range (FSR) for different optical path length differences (ΔL)

$\Delta L (\mu\text{m})$	FSR (nm)
10	57.15
50	11.43
100	5.715
150	3.81
200	2.86

C. Photonic Circuit Transmission Spectrum

The transmission spectrum of the designed MZI circuit is simulated using Lumerical INTERCONNECT. This simulation provides the expected optical response of the device, which can then be compared with experimental measurements.

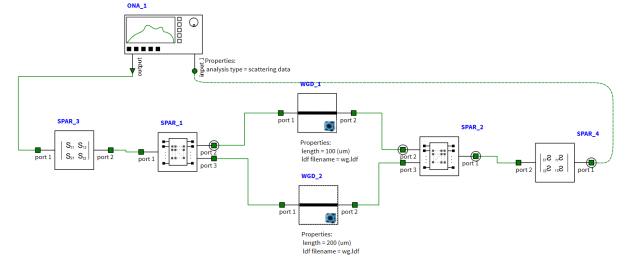


Fig. 7: Schematic of MZI compact mode

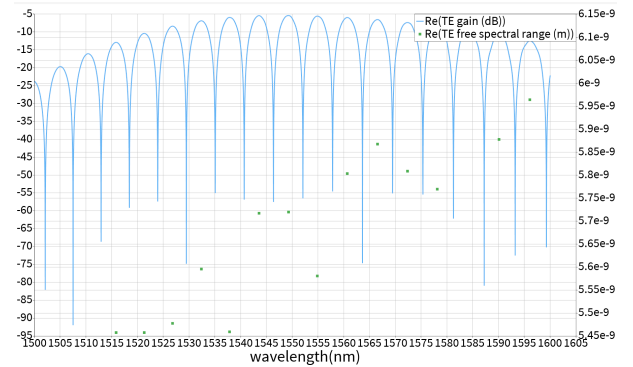


Fig. 8: Response of MZI

IV. FABRICATION- WASHINGTON NANOFABRICATION FACILITY (WNF) SILICON PHOTONICS PROCESS

The devices were fabricated using 100 keV electron beam lithography [1]. The fabrication used a silicon-on-insulator

wafer with a 220 nm thick silicon layer on a 3 μm thick buried oxide. The substrates were 25 mm squares diced from 150 mm wafers. After a solvent rinse and a hot-plate dehydration bake, hydrogen silsesquioxane resist (HSQ, Dow-Corning XP-1541-006) was spin-coated at 4000 rpm and baked at 80 $^{\circ}\text{C}$ for 4 minutes.

Electron beam lithography was performed using a JEOL JBX-6300FS system operated at 100 keV, with a beam current of 8 nA and an exposure field size of 500 μm . The machine grid for shape placement was 1 nm, and the beam stepping grid (the spacing between dwell points) was 6 nm. An exposure dose of 2800 $\mu\text{C}/\text{cm}^2$ was used.

The resist was developed by immersion in 25 % tetramethylammonium hydroxide (TMAH) for 4 minutes, followed by a deionized water rinse for 60 s, an isopropanol rinse for 10 s, and drying with nitrogen gas.

Unexposed silicon was etched using inductively coupled plasma (ICP) etching in an Oxford Plasmalab System 100. The process used a chlorine gas flow of 20 sccm, pressure of 12 mTorr, ICP power of 800 W, RF bias power of 40 W, and platen temperature of 20 $^{\circ}\text{C}$, resulting in a bias voltage of 185 V. During etching, chips were mounted on a 100 mm silicon carrier wafer using perfluoropolyether (PFPE) vacuum oil.

Cladding oxide was deposited using plasma-enhanced chemical vapor deposition (PECVD) in the same Oxford Plasmalab System 100. Process parameters included a silane (SiH_4) flow of 13.0 sccm, nitrous oxide (N_2O) flow of 1000.0 sccm, nitrogen (N_2) flow of 500.0 sccm, chamber pressure of 1400 mTorr, high-frequency RF power of 120 W, and platen temperature of 350 $^{\circ}\text{C}$. During deposition, the chips were placed directly on a silicon carrier wafer and buffered on all sides by silicon pieces to improve uniformity.

V. EXPERIMENT DATA

To characterize the devices, a custom-built automated test setup [2], [3] with automated control software written in Python was used [3]. An Agilent 81600B tunable laser was used as the input source and Agilent 81635A optical power sensors as the output detectors. The wavelength was swept from 1500 to 1600 nm in 10 pm steps. A polarization-maintaining (PM) fibre was used to maintain the polarization state of the light, to couple the TE polarization into the grating couplers [4]. A 90 $^{\circ}$ rotation was used to inject light into the TM grating couplers [4]. A polarization-maintaining fibre array was used to couple light in/out of the chip [5].

VI. ANALYSIS

A. Corner Analysis

Objective: Update the model (waveguide, interferometer) to take into account manufacturing variations. Re-simulate the circuit for anticipated variations. Determine the impact of the variations on the following device & circuit parameters: waveguide effective index (n_{eff}) and group index (n_g), free-spectral range (FSR).

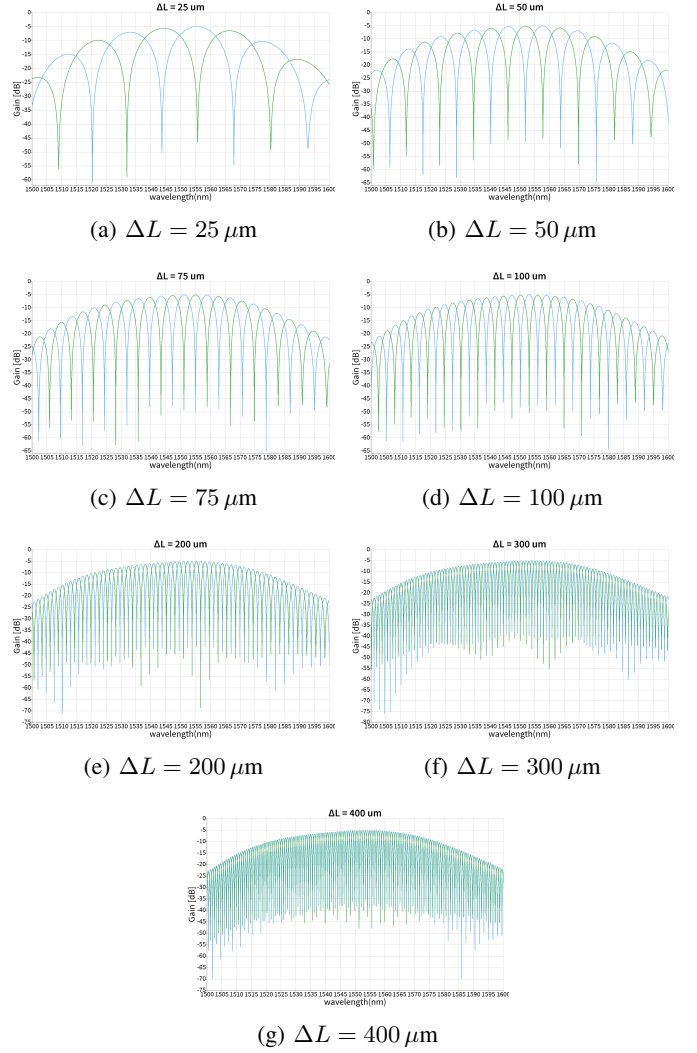


Fig. 9: Experimental results for varying optical path length differences (ΔL).

Manufacturing challenges, particularly variations in waveguide dimensions (height and width), can significantly impact the optical properties of integrated photonic devices. To understand and quantify this impact, a corner analysis was performed. This analysis involves simulating the waveguide and MZI performance at the extreme limits of expected fabrication tolerances for width (w) and height (h). Specifically, four corners were considered:

- Nominal: $w = 500 \text{ nm}$, $h = 220 \text{ nm}$
- Corner 1 (Min Width, Max Height): $w = w_{\text{min}}$, $h = h_{\text{max}}$
- Corner 2 (Max Width, Min Height): $w = w_{\text{max}}$, $h = h_{\text{min}}$
- Corner 3 (Min Width, Min Height): $w = w_{\text{min}}$, $h = h_{\text{min}}$
- Corner 4 (Max Width, Max Height): $w = w_{\text{max}}$, $h = h_{\text{max}}$

(Specify the actual $w_{\text{min/max}}$ and $h_{\text{min/max}}$ values here, e.g., $\pm 10 \text{ nm}$ for width and $\pm 5 \text{ nm}$ for height).

For each corner, the waveguide effective index (n_{eff}) and group index (n_g) were simulated across the wavelength range of interest. The results, as shown in Figure ??, indicate

that variations in waveguide dimensions lead to noticeable shifts in both n_{eff} and n_g curves. For instance, a decrease in waveguide width typically leads to a lower effective index and a higher group index due to stronger confinement and dispersion effects.

The impact on the MZI's Free Spectral Range (FSR) was also determined for each corner. Since FSR is inversely proportional to $n_g \Delta L$, changes in n_g directly translate to variations in FSR. Table II summarizes the FSR values obtained for a specific ΔL (e.g., $100\mu\text{m}$) at each corner. These results highlight the range of FSR values that can be expected from fabricated devices due to manufacturing tolerances.

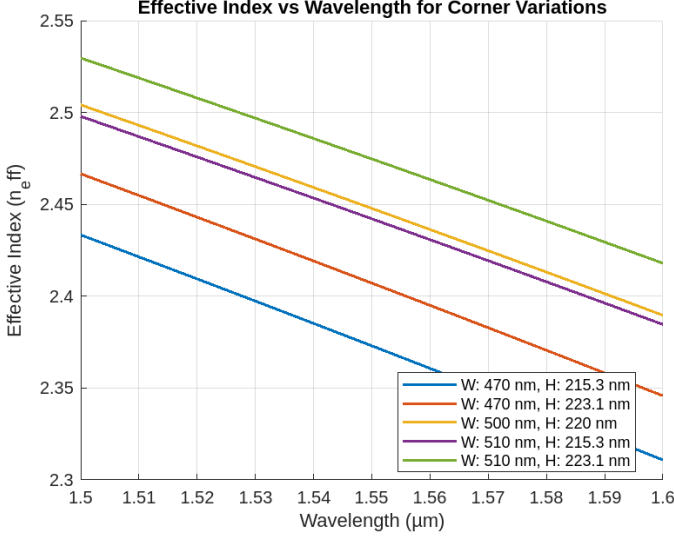


Fig. 10: Effective Index variation for Corner Analysis

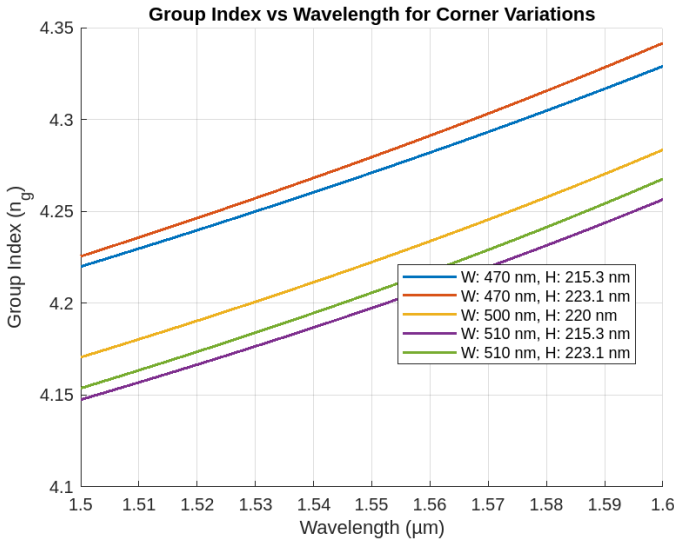


Fig. 11: Group Index variation for Corner Analysis

B. Monte Carlo Simulation

Objective: This unit demonstrates how to perform Monte Carlo simulations directly from the layout. This function

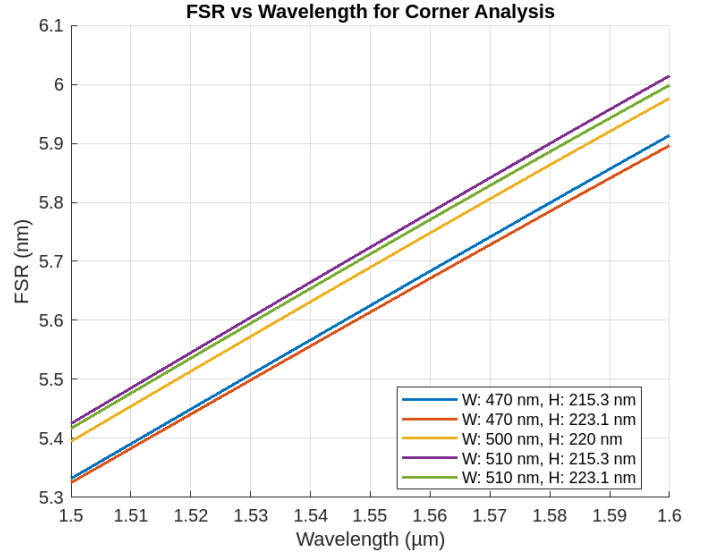


Fig. 12: Free Spectral Range variation for Corner Analysis

TABLE II: Impact of Corner Analysis on FSR for $\Delta L = 100\mu\text{m}$

Waveguide Parameters	Value (nm)	FSR (nm)
Minimum Width, Minimum Height	470, 215.3	5.618
Minimum Width, Maximum Height	470, 223.1	5.607
Nominal	500, 220	5.6825
Maximum Width, Minimum Height	500, 215.3	5.716
Maximum Width, Maximum Height	500, 223.1	5.705

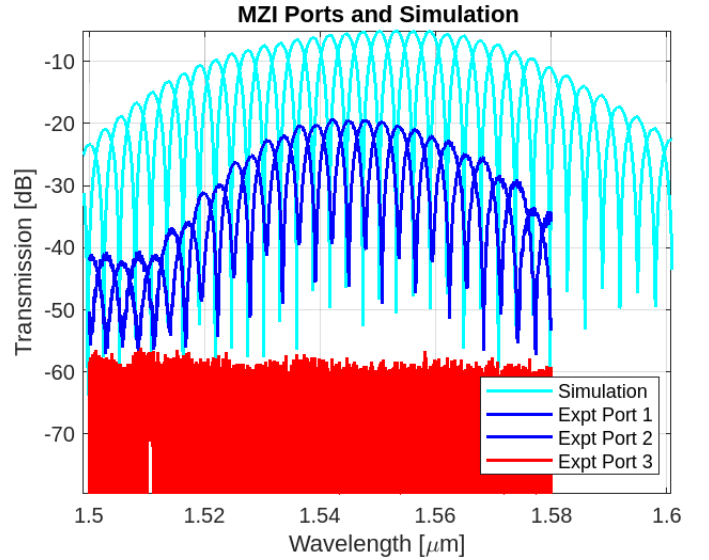


Fig. 13: Enter Caption

is available in KLayout and uses the compact models we developed for the Lumerical INTERCONNECT circuit solver.

To gain a more comprehensive statistical understanding of the impact of manufacturing variations, Monte Carlo simulations were performed. This approach involves randomly sampling waveguide parameters (e.g., width and height) within

their defined statistical distributions (e.g., Gaussian distribution with a specified mean and standard deviation) and then simulating the device performance for each sample. This process was executed directly from the KLayout layout using the integrated compact models for Lumerical INTERCONNECT.

The simulation results provide histograms for key device and circuit parameters, such as waveguide effective index (n_{eff}), group index (n_g), and MZI FSR. These histograms (e.g., Figure ??) visually represent the distribution of these parameters across many fabrication runs. By inspecting the mean and standard deviation values of these distributions, we can quantify the expected variability and assess the manufacturing yield of the designed devices. For instance, the mean FSR was found to be 5.77 nm with a standard deviation of 0.155 nm for a specific MZI design.

During the Monte Carlo simulations, it was observed that some simulation runs might produce non-physical results (e.g., infinities or NaN values) due to extreme parameter combinations or simulation convergence issues. In such cases, the dataset was "cleaned" by filtering out these invalid entries, and the data was re-plotted using the analysis scripts (e.g., KLayout-generated '.lsf' script) to ensure the histograms and statistical metrics are accurate and representative of valid device performance. This robust analysis provides critical insights into the design's robustness against manufacturing imperfections.

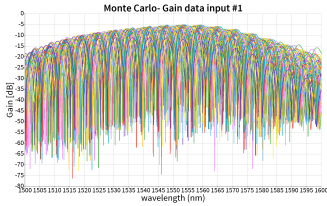


Fig. 14: Enter Caption for MC_gain1

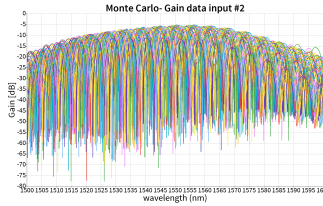


Fig. 15: Enter Caption for MC_gain2

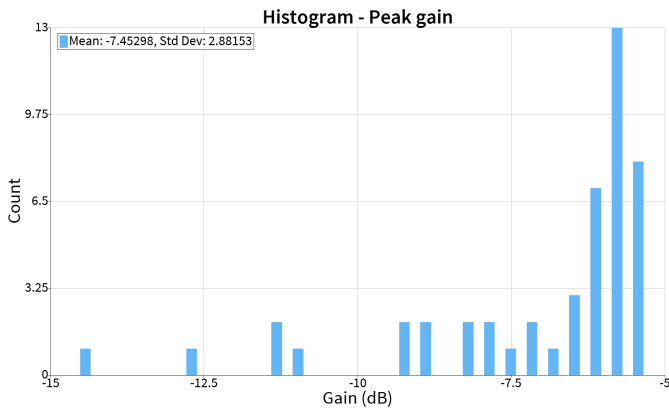


Fig. 16: Enter Caption

C. Auto-Correlation Analysis

To achieve a closer match between simulation and experiment, the experimental data is fitted using the MZI transfer

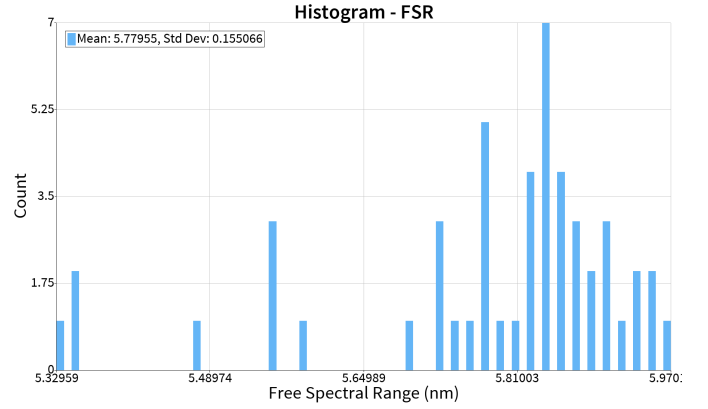


Fig. 17: Enter Caption

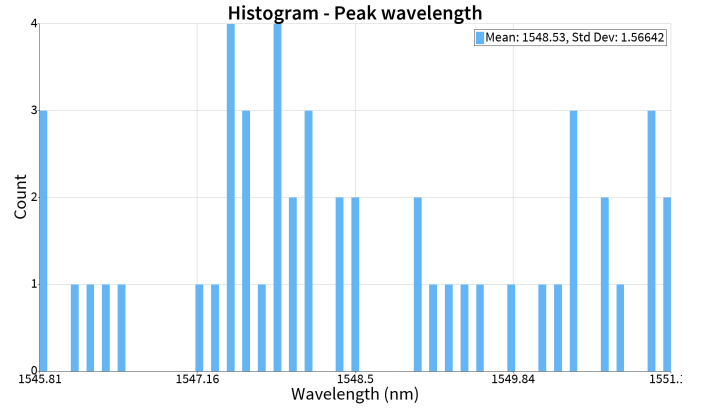


Fig. 18: monte carlo histograms

function compact model. This process involves optimizing the model parameters (n_1, n_2, n_3 , propagation loss α , and an amplitude offset) to minimize the difference between the model output and the measured data. The MATLAB code provided previously facilitates this fitting process, employing a least-squares curve fitting algorithm. The fitting allows for the extraction of effective waveguide parameters that best describe the fabricated device.

The MZI transfer function used for fitting is given by:

$$T_{\text{MZI}}(X, \lambda) = 10 \log_{10} \left(0.25 \left| 1 + e^{-i\beta(X_{1:3}, X_4, \lambda) \Delta L} \right|^2 \right) + X_5 \quad (1)$$

where $X = [n_1, n_2, n_3, \alpha, \text{offset}]$ are the fitting parameters, β is the complex propagation constant, and ΔL is the path length difference.

The results of the fitting process, showing the excellent agreement between the fitted model and the experimental data, are presented in Figure ?. The fitted curve closely follows the experimental oscillations, indicating a successful parameter extraction.

VII. CONCLUSION

The proposal outlines the simulation of Mach-Zehnder interferometer circuit using a Y-branch splitter-combiner. The

results show that the FSR obtained through simulation which is closest to 1550 nm wavelength is around 5.719 nm which verifies the theoretical calculation at a path length difference of 100 μm . The next steps involve translating these designs into a detailed layout file (GDSII format) for submission to fabrication, followed by experimental testing and comprehensive analysis of the results upon receiving the fabricated chips.

ACKNOWLEDGMENT

We acknowledge the edX UBCx Phot1x Silicon Photonics Design, Fabrication and Data Analysis course, which is supported by the Natural Sciences and Engineering Research Council of Canada (NSERC) Silicon Electronic-Photonic Integrated Circuits (SiEPIC) Program. The devices were fabricated by Richard Bojko at the University of Washington Washington Nanofabrication Facility, part of the National Science Foundation's National Nanotechnology Infrastructure Network (NNIN), and Cameron Horvath at Applied Nanotools, Inc. Omid Esmaeeli performed the measurements at The University of British Columbia. We acknowledge Lumerical Solutions, Inc., Mathworks, Mentor Graphics, Python, and KLayout for the design software.

Additionally, we extend our gratitude to Pramatra Tech Services (India) Private Limited for their support throughout the duration of the course.

REFERENCES

- [1] R. J. Bojko, J. Li, L. He, T. Baehr-Jones, M. Hochberg, and Y. Aida, "Electron beam lithography writing strategies for low loss, high confinement silicon optical waveguides," *Journal of Vacuum Science & Technology B*, vol. 29, no. 6, 2011.
- [2] PLC Connections, "PLC Connections Website." <http://www.plcconnections.com>, 2025. Accessed: July 8, 2025.
- [3] M. Caverley, "SiEPIC Probe Station." <http://siepic.ubc.ca/probestation>. Python code developed by Michael Caverley; Accessed: July 8, 2025.
- [4] L. Chrostowski and M. Hochberg, *Silicon photonics design: from devices to systems*. Cambridge University Press, 2015.
- [5] Maple Leaf Photonics, "Maple Leaf Photonics Website." <http://mapleleafphotonics.com>, 2025. Accessed: July 8, 2025.